








Cite this: *Nanoscale*, 2017, **9**, 11170

## The origin of high electrocatalytic activity of hydrogen peroxide reduction reaction by a g-C<sub>3</sub>N<sub>4</sub>/HOPG sensor

C. G. Gomez, \*<sup>a</sup> A. M. Silva, <sup>b</sup> M. C. Strumia, <sup>a</sup> L. B. Avalle <sup>c</sup> and M. I. Rojas \*<sup>d</sup>

Graphitic carbon nitride (g-C<sub>3</sub>N<sub>4</sub>) was synthesized from a low-cost precursor by means of a thermal process. The product was characterized by several spectroscopic techniques and the crystallinity was analyzed by X-ray diffraction. In the manufacture of the sensor, g-C<sub>3</sub>N<sub>4</sub> was chemically exfoliated and a film was placed on the surface of a Highly Oriented Pyrolytic Graphite (HOPG). We compared the electrocatalytic activities of g-C<sub>3</sub>N<sub>4</sub>/HOPG and pristine HOPG surfaces as sensors for H<sub>2</sub>O<sub>2</sub> quantification in buffer solution at pH 7. The results indicate that the surface of g-C<sub>3</sub>N<sub>4</sub>/HOPG exhibits striking analytical stability as well as reproducibility, enabling a reliable and sensitive determination within the 0.12–120 μM interval with a detection limit of 0.12 μM. These results suggest that this g-C<sub>3</sub>N<sub>4</sub> film is a really particularly good nano-structured material to be applied as a biosensor. Chemical and physical factors are responsible for the outstanding electrocatalytic activity observed. The N in the g-C<sub>3</sub>N<sub>4</sub> allows huge uptake of H<sub>2</sub>O<sub>2</sub> through the hydrogen-bonding interaction and the change in the electronic structure since the HOPG/g-C<sub>3</sub>N<sub>4</sub> heterojunction favors the charge transfer process through the interface.

Received 17th April 2017,  
Accepted 12th July 2017  
DOI: 10.1039/c7nr02736b

rsc.li/nanoscale

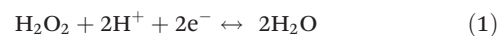
## Introduction

Graphitic materials are suitable for the manufacture of biosensors to quantify molecules of biological interest, due to their high specific surface area. Graphitic carbon nitride is a new class of carbonaceous materials doped with N atoms.<sup>1–6</sup> The tri-s-triazine based-connection pattern is the most stable allotrope of g-C<sub>3</sub>N<sub>4</sub> under ambient conditions.<sup>1–3</sup> Since N and C atoms belong to different groups of the periodic table, they form different numbers of bonds which, in the honeycomb lattice, gives rise to a periodic distribution of pores.<sup>7</sup> Since carbon nitride is mainly composed of C and N atoms, among the most abundant elements, it is also being considered an environmentally friendly material. It can be synthesized at low

cost by the polymerization of N-rich precursors like cyanamide, dicyandiamide and melamine,<sup>3</sup> obtaining a highly textured and graphitic organized polymeric material. The lattice parameter is 7.14 Å and the sheets are stacked with an interplanar distance of 3.25 Å.<sup>5–7</sup> As N and C atoms have different electronegativities, the C–N bonds are polar, where N is positively and C is negatively charged.<sup>7</sup> In reference to the electrical properties, it is an n-type organic semiconductor with an indirect band gap of 1.90 eV.<sup>7</sup>

This N-doped carbonaceous material has a high electrocatalytic activity.<sup>8–10</sup> Taking into account its high sensitivity, good selectivity and ease of operation, g-C<sub>3</sub>N<sub>4</sub> may be used in the manufacture of sensors.<sup>4,11</sup> On the other hand, the H<sub>2</sub>O<sub>2</sub> molecule is the product of several biological enzyme-catalyzed reactions and its detection and quantification play an important role in the food industry, environmental protection and medical diagnoses.<sup>12,13</sup> Among the different techniques used to detect H<sub>2</sub>O<sub>2</sub>, the electrochemical method has the advantage of being simple, with low cost and great sensitivity as well as selectivity.

The electro-catalytic activity of HOPG and g-C<sub>3</sub>N<sub>4</sub>/HOPG surfaces for HP RR takes place, according to the following equation:



Although the electrolyte has pH 7, the reduction of H<sub>2</sub>O<sub>2</sub> (HP RR) is considered to occur in an acid medium since the

<sup>a</sup>IPQA-CONICET, Departamento de Química Orgánica, Facultad de Ciencias Químicas, Universidad Nacional de Córdoba, Edificio Ciencias II, Haya de la Torre y Medina Allende, (5000) Córdoba, Argentina. E-mail: gom@fcq.unc.edu.ar;

Tel: +54 351 5353867 int. 53343

<sup>b</sup>Divisão de Metrologia de Materiais, (INMETRO) Instituto Nacional de Metrologia, Normalização e Qualidade Industrial, Duque de Caxias, Rio de Janeiro, RJ 25245-020, Brazil

<sup>c</sup>IFEG-CONICET, Facultad de Matemática, Astronomía, Física y Computación, Universidad Nacional de Córdoba, Ciudad Universitaria, 5000 Córdoba, Argentina

<sup>d</sup>INFIQC-CONICET, Departamento de Química Teórica y Computacional, Facultad de Ciencias Químicas, Universidad Nacional de Córdoba – Ciudad Universitaria, 5000 Córdoba, Argentina. E-mail: mrojas@fcq.unc.edu.ar;

Tel: +54 351 5353853 int. 55186

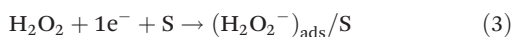
reaction takes place on the cathode surface. Thus, there is a high  $[H^+]$  concentration at the interface, even though it is lower in the solution.

Recently, Rojas *et al.*<sup>14</sup> have studied the  $H_2O_2$  adsorption and its reduction on graphene by means of theoretical calculation. The adsorption energy was  $-0.051$  eV (physisorption). The slow step was the cleavage of the O–O bond with an energy barrier of 1.00 eV for the Stone–Wale defective site<sup>15</sup> and 1.70 eV for the normal site.

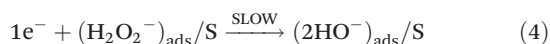
The following mechanism of consecutive reactions involves two single electrochemical species, considered as follows:



The first step is a reductive  $H_2O_2$  adsorption on the surface (S):



It is followed by a reductive dissociation of  $H_2O_2$ :



Eqn (4) is the rate-determining step for HPRR, due to the fact that O–O cleavage generally has an important energy barrier. Finally, adsorbed hydroxyl groups are protonated to give two desorbed water molecules:



The rate of eqn (3) depends on the vacancies of surface sites, while the rate of eqn (4) depends on the content of  $H_2O_2$  adsorbed onto the surface.

On the surface of both kinds of electrodes, HPRR takes place through a mechanism involving (3–5) elementary steps. The catalytic activity of each surface depends on the energy barrier of the (4) step.

In this work, we performed the synthesis of  $g-C_3N_4$  by a thermal process of a low-cost precursor such as melamine. This product was then characterized by spectroscopic techniques and the crystallinity was analyzed by X-ray diffraction. After that, a  $g-C_3N_4$  sample was chemically exfoliated and deposited on the HOPG surface to be used as an electrochemical sensor. Finally, the surfaces of  $g-C_3N_4$ /HOPG and HOPG were tested by electrochemical techniques for quantification of a low concentration of  $H_2O_2$  in buffer solution at pH 7.

## Experimental details

### Reagents and equipment

Reagents were used as purchased. Melamine >99 wt% Merck, (Switzerland);  $H_2SO_4$  98 wt%, Cicarelli (Argentina);  $NaHCO_3$  p.a., Cicarelli (Argentina); 0.20 M phosphate buffer pH 7, Anedra (Argentina); HCl 37 wt%, Cicarelli (Argentina); ethanol 96 vol%, Porta (Argentina);  $H_2O_2$  30 vol%, Cicarelli (Argentina).

Spectrophotometric measurements were performed on a Shimadzu UV-Visible spectrophotometer UV -1800, UV Probe 2.30 (Japan).

Fourier-transform infrared (FTIR) spectra of samples were obtained by using a Nicolet iN10 spectrometer (USA).

Determination of pH was carried out by using a digital pH meter Altronix, TPXI 1584 (Argentina).

Transmission electron microscopy (TEM) was performed by using a JEOL-JEM 1200 EXII instrument (USA).

Scanning Electron Microscopy with a field emission gun (SEM-FEG) was performed using a microscope SIGMA HD-CARLS ZEISS (Germany).

X-Ray Diffraction (XRD) patterns were obtained at room temperature on a PAN Analytical X-Pert Pro diffractometer (40 kV, 40 mA) in Bragg–Brentano geometry with Cu  $K\alpha$  radiation in the range of 10 to 100° with a step size of 0.02° and a step counting time of 10 s (Netherland).

Energy Dispersive X-ray Spectroscopy (EDS) was performed with an Energy Dispersive Spectrometer attached to the SEM, consisting of a silicon drift Oxford detector with an Aztec characterization system.

The electrochemical analyser used was a Metrohm AUTOLAB- PGSTAT302N potentiostat (Switzerland) equipped with a staircase scan module and an electrochemical interface using the NOVA 2.01 software package.

### Synthesis of $g-C_3N_4$ and methods

An allotrope of  $g-C_3N_4$  constituted by a polymer based on tri-s-triazine units was successfully synthesized by a melamine thermal process using an electrical oven (Model 332 INDEF, Argentina). This reagent (8.00 g) was introduced into a porcelain cup and left into the oven for reaction (Fig. 1). The thermal treatment used had a heating rate of 2 °C  $min^{-1}$  from 25 °C to 550 °C, kept constantly for 4 h.

Afterwards, the  $g-C_3N_4$  was chemically exfoliated. A sample (0.20 g) of  $g-C_3N_4$  synthesized was mixed with a 0.50 M  $H_2SO_4$  aqueous solution (400 mL) and then left under sonication for 30 min, from which a yellow suspension was obtained (Fig. 1). After that, this suspension was mixed with a 96 vol% ethanol in volume proportion (50:50) and the exfoliated  $g-C_3N_4$  suspension was precipitated by centrifugation at 7000 rpm.

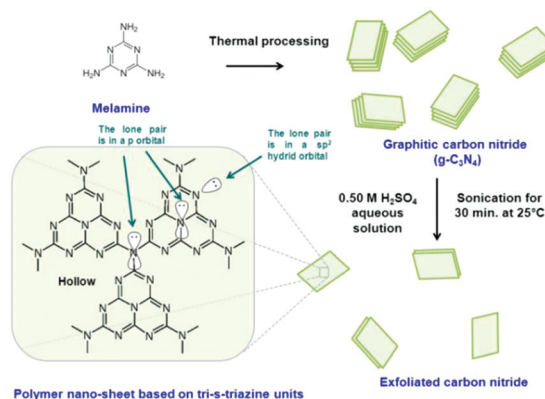


Fig. 1 From precursor to polymer synthesis and the chemical exfoliation process.

The exfoliated  $g\text{-C}_3\text{N}_4$  sample was suspended with 10 mL of an ethanol/water mixture (70 : 30) under sonication for 15 min and separated from the supernatant by centrifugation. This process was performed three times. Finally, a 0.033 wt%  $g\text{-C}_3\text{N}_4$  ethanol suspension after 20 min of sonication was attained and characterized by UV-Vis spectrometry.

In addition, one drop of the  $g\text{-C}_3\text{N}_4$  ethanolic suspension was seeded twice on the sample holder grid for TEM, and then dried at 25 °C. Similarly, a  $g\text{-C}_3\text{N}_4$  sample was deposited on the carbon tape/sample holder, then gold-plated and characterized by Scanning Electron Microscopy/Energy-Dispersive Ray-X Spectroscopy (SEM/EDS).

### Electrochemical measurements

A conventional electrochemical cell of three electrodes was used, consisting of a working electrode, an Ag/AgCl reference electrode and a gold rod (Alfa Aesar 99.9985% purity) auxiliary electrode. The auxiliary electrode was cleaned by annealing in butane flame during 2 min, cooled under  $\text{N}_2$  flux, and immediately placed in contact with the electrolytic solution. Oxygen-free solutions were obtained by continuously purging the electrochemical cell with nitrogen gas (99.999% purity). Water from a Milli-Q Millipore System was used for the preparation of all solutions and for glassware cleaning. All chemicals were of analytical grade. The working electrode used was a  $7 \times 7 \text{ mm}^2$  HOPG, mechanically exfoliated with the adhesive tape method. In the case of the  $g\text{-C}_3\text{N}_4$ /HOPG surface, the film was placed by dripping the  $g\text{-C}_3\text{N}_4$  ethanolic suspension on the HOPG surface (8 drops), followed by ethanol evaporation at 25 °C.

### Cyclic voltammetry

The working electrodes were transferred to the electrochemical cell with a drop of ultrapure water. The measurements for blank experiments were performed in buffer pH 7 cycling in the range  $[-1, 0.4] \text{ V vs. Ag/AgCl}$  reference electrode at  $0.050 \text{ V s}^{-1}$ . Different aliquots of 50  $\mu\text{L}$  of a stock solution of the  $\text{H}_2\text{O}_2$  analyte were injected into the 50 mL electrochemical cell to give various final  $\text{H}_2\text{O}_2$  concentrations in the bulk solution. The potentiodynamic current density – potential ( $j$ - $E$ ) profiles were recorded after each addition under steady-state conditions.

### Current transients

Stabilization of the system was performed by applying an initial potential,  $V_i$ , of  $-0.40 \text{ V}$ . A potential step at a more negative potential value,  $V_{trans}$ , of  $-0.6 \text{ V}$  was then applied recording the current as a function of time. Afterwards, the potential was returned to the initial value. This procedure allowed verifying the interface stability after a kinetic of potential variation was used. Voltammogram comparisons obtained under steady-state conditions before and after analyte addition were made to determine the  $V_{trans}$  value.

### Impedance measurements

The amplitude of the  $ac$  perturbation signal was 10 mV and the frequency range scanned was 0.1 Hz–100 kHz for HPRR at  $-0.6 \text{ V vs. Ag/AgCl}$  as a reference electrode.

### Model and computations

The optimized lattice parameter for the  $g\text{-C}_3\text{N}_4$ /graphene bilayer was 7.29 Å. The first sheet, the tri-s-triazine one, was composed of 8 N and 6 C atoms; the second sheet, the graphene one, had 18 C atoms. The atoms in both layers were arranged in a honeycomb lattice. The unit cell was tetrahedral of  $7.29 \text{ Å} \times 7.29 \text{ Å} \times 30 \text{ Å}$  with periodic boundary conditions in the  $x$ ,  $y$ , and  $z$  directions imposed in order to represent an infinite surface.

All DFT calculations were performed using the Quantum Espresso package<sup>16</sup> with van der Waals interactions. The Kohn–Sham orbitals and charge density were expanded in plane-wave basis sets up to a kinetic energy cutoff of 60 and 480 Ry for all atoms. Ultrasoft pseudopotentials were employed with the Perdew–Burke–Ernzerhof approximation for exchange and correlation in the PBE functional.<sup>17,18</sup> The BZ was sampled with a  $4 \times 4 \times 1$  irreducible Monkhorst–Pack  $k$ -point grid.<sup>19</sup> The convergence threshold for the total energy at each electronic calculation was set to  $1 \times 10^{-8}$  Ry. Geometry optimizations were performed employing the Broyden–Fletcher–Goldfarb–Shanno (BFGS) algorithm (for stress minimization) and total forces acting on each ion are minimized to reach less than  $1 \times 10^{-3}$  Ry a.u.<sup>-1</sup> by movement of the ionic positions.

## Results and discussion

### Synthesis and characterization of $g\text{-C}_3\text{N}_4$

Synthesis of  $g\text{-C}_3\text{N}_4$  by thermal treatment of a low-cost precursor such as melamine was performed with a yield of 75 wt% at 550 °C for 4 h (ref. 3) (see Fig. 1). After that, a sample of synthesized  $g\text{-C}_3\text{N}_4$  was characterized by spectroscopic techniques. Fig. 2(A) shows a photograph of a sample of  $g\text{-C}_3\text{N}_4$  where, at first sight, this material is composed of yellow dust together with irregular particles of diameters near 3 mm and a low apparent density. These properties agree with those found in the material reported by other authors.<sup>3,4</sup> In addition, Fig. 2(B) shows a micrograph of SEM of an exfoliated  $g\text{-C}_3\text{N}_4$  sample, where the surface is composed of stacked nanosheets in the presence of terraces and steps.

Fig. 2(C) shows the profile of the FTIR spectrum of a  $g\text{-C}_3\text{N}_4$  sample, which exhibits different bands. The signal at  $3250 \text{ cm}^{-1}$  is attributed to stretching  $\nu$  N–H, while that at

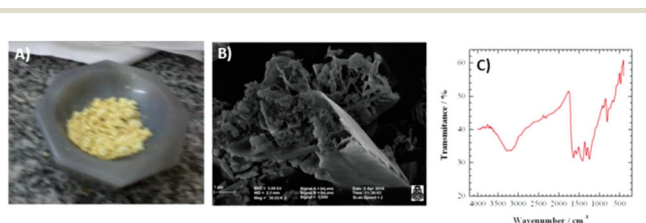
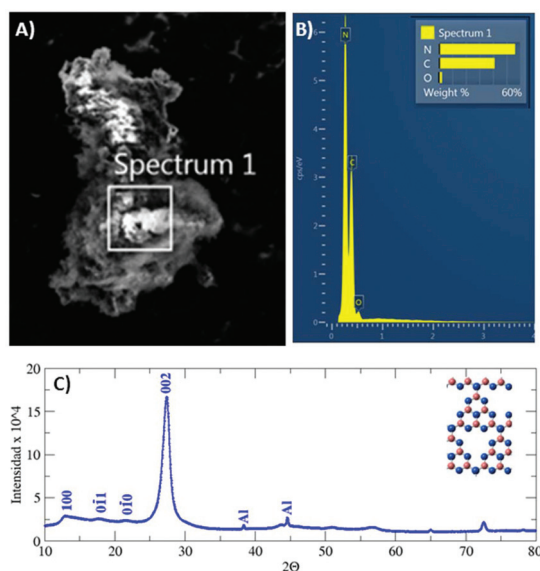


Fig. 2 (A) The photograph shows the texture of the yellow crystals of synthesized  $g\text{-C}_3\text{N}_4$ ; (B) SEM image shows the agglomerates of porous solids; (C) FTIR:  $\nu$ N–H  $3250 \text{ cm}^{-1}$ ,  $\nu$ C=C or  $\nu$ C=N  $1630 \text{ cm}^{-1}$  stretching and  $\sigma$ C–N aromatic heterocyclic ring twisting  $805 \text{ cm}^{-1}$ .



**Fig. 3** (Above) crystal morphology and EDS composition of the g-C<sub>3</sub>N<sub>4</sub> crystal synthesised. The square is of 10 μm of sideways. (Down) X-ray diffraction pattern (XRD) shows a crystalline structure. The 002 plane is located at 27.4°, corresponding to the inter-planar distance of 3.25 Å. Inset: Arrangement of atoms in a layer, blue spheres are N atoms; red spheres are C atoms.

1630 cm<sup>-1</sup> corresponds to  $\nu$  C=C or  $\nu$  C=N, these characteristic bands being typical of the tri-s-triazine allotrope.<sup>20</sup> In addition, the flexion signal  $\sigma$  C-N of aromatic heterocyclic ring twisting appears at 805 cm<sup>-1</sup>.

Fig. 3 shows the morphology and composition of a g-C<sub>3</sub>N<sub>4</sub> crystal obtained by Energy Dispersive X-ray Spectroscopy (EDS). From the EDS analysis, it is found that C and N content mainly agrees with the C<sub>3</sub>N<sub>4</sub> formula. This graphite kind normally has a crystalline structure, which has been studied through X-ray diffraction patterns (XRD). The inter-layer distance can be experimentally determined through the angles at which the diffraction peak appears according to Bragg's Law:<sup>21</sup>

$$n\lambda = 2d \cdot \sin \theta \quad (6)$$

where  $2d \cdot \sin \theta$  is the path difference between the two rays,  $\theta$  is the angle of incidence and the integer  $n$  is the order of the corresponding reflection peak.

Fig. 3(Down) shows the XRD pattern of the g-C<sub>3</sub>N<sub>4</sub> sample. The 002 peak appears at 27.4° corresponding to an inter-planar distance of 3.25 Å. The peak is that of the highest intensity and it is also sharp indicating that the synthesis product is crystalline. Low angles such as 100, 011, and 010 are characteristic peaks of the tri-s-triazine structure<sup>3,4,7,22,23</sup> which depend on the arrangement of atoms in the layer. The inset of Fig. 3 shows the arrangement of atoms. Table 1 lists Miller indexes, angles at which the corresponding distance of the pattern observed are seen. In addition, other peaks are found, corresponding to the aluminium sample holder used in the characterization.

**Table 1** *hkl* plane assignment, the angles, the plane distance and the material

<i>hkl</i>	$2\theta$ [°]	$d$ [Å]	Material
100	12.9	6.83	g-C <sub>3</sub> N <sub>4</sub>
011	17.8	4.98	g-C <sub>3</sub> N <sub>4</sub>
010	21.6	4.10	g-C <sub>3</sub> N <sub>4</sub>
002	27.4	3.25	g-C <sub>3</sub> N <sub>4</sub>
111	38.4	2.34	Al
	43.7	2.07	g-C <sub>3</sub> N <sub>4</sub>
200	44.6	2.03	Al
	50.9	1.79	g-C <sub>3</sub> N <sub>4</sub>
	56.8	1.62	g-C <sub>3</sub> N <sub>4</sub>
	65.0	1.43	g-C <sub>3</sub> N <sub>4</sub>
	72.5	1.30	g-C <sub>3</sub> N <sub>4</sub>
	78.2	1.22	g-C <sub>3</sub> N <sub>4</sub>

### Adsorption of the g-C<sub>3</sub>N<sub>4</sub> film on the HOPG surface

g-C<sub>3</sub>N<sub>4</sub> nanosheets were obtained from chemical exfoliation of the synthesized product assisted by ultra-sonication (Fig. 1).<sup>24,25</sup> The N atom in the structure in a 0.5 M H<sub>2</sub>SO<sub>4</sub> aqueous solution was protonated, yielding sheets positively charged. These were repulsed with each other, which led to a chemical exfoliation accelerated by sonication. After that, exfoliated g-C<sub>3</sub>N<sub>4</sub> nanosheets were placed onto the HOPG surface from an ethanolic g-C<sub>3</sub>N<sub>4</sub> suspension, drop by drop. Following ethanol evaporation, a g-C<sub>3</sub>N<sub>4</sub> film was attained.

Fig. 4(A) shows the UV-Visible spectrum of an aqueous suspension of the exfoliated g-C<sub>3</sub>N<sub>4</sub> at pH 3 and pH 9. The profile of spectral curves agrees with that found by Das *et al.*,<sup>26</sup> which supports the formation of g-C<sub>3</sub>N<sub>4</sub>. In both cases, two bands near 320 and 370 nm were observed, which was related to the existence of a conjugated  $\pi$  system.

This phenomenon supports the fact that the g-C<sub>3</sub>N<sub>4</sub> polymer has an aromatic structure based on interconnected tri-s-triazine units where their atoms have sp<sup>2</sup> hybridization. Taking into account the different environments, three different types of N atoms were observed: a N atom, with lone pair electrons in a sp<sup>2</sup> orbital, and two different types of N atoms with a lone pair in p orbitals (Fig. 1).

Fig. 4(B) shows a Transmission Electron Microscopy (TEM) image of exfoliated g-C<sub>3</sub>N<sub>4</sub>, where micro-crystals of few sheets of thickness can be observed.

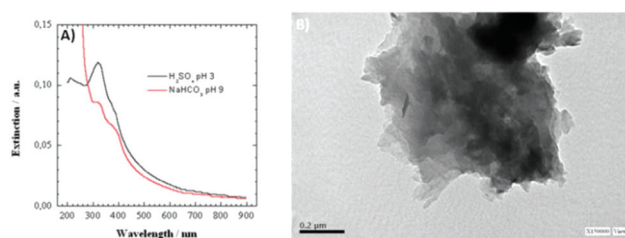


**Fig. 4** g-C<sub>3</sub>N<sub>4</sub> exfoliated. (A) UV-Visible Spectroscopy and (B) TEM image shows microcrystals of a few sheets of thickness.



### Cyclic voltammetry (CV) and chronoamperometry (CA)

We compared the electrochemical properties and performance of HOPG and g-C<sub>3</sub>N<sub>4</sub>/HOPG electrodes by CV and CA.

The CA  $j(t)$ -time response is related to the number of adsorption sites on the cathode surface taking into account the mechanism proposed and the kinetics for each step. In the HPRR mechanism, there are two reduction steps (3–4) followed by a protonation step (5) and a site release. Only the reduction steps (3–4) contribute to the cathodic  $j(t)$ . Thus, the  $j(t)$  value responses to a potential step for HPRR, neglecting the double layer charging, can be approached as follows:

$$j(t) = n_1 F k_1 (1 - \theta(t)) + n_2 F k_2 \theta(t). \quad (7)$$

Two terms of eqn (7) have rate constants  $k_1(\eta, C_{\text{H}_2\text{O}_2})$  and  $k_2(\eta, C_{\text{H}_2\text{O}_2})$ , which depend on the over-potential applied ( $\eta$ ) and the H<sub>2</sub>O<sub>2</sub> concentration ( $C_{\text{H}_2\text{O}_2}$ ) in the solution. Thus, kinetics of H<sub>2</sub>O<sub>2</sub> adsorption (eqn (3)) depends on the number of free sites on the surface ( $1 - \theta(t)$ ), while cleavage of the O–O bond depends on the number of adsorbed molecules  $\theta(t)$ .

The  $j(t)$ -time response for a planar electrode surface is related to the  $C_{\text{H}_2\text{O}_2}$  by means of the Cottrell equation,<sup>27</sup> applied to a diffusion-controlled process:

$$|j(t)| = nF \sqrt{\frac{D_{\text{O}}}{\pi}} t^{-1/2} C_{\text{H}_2\text{O}_2} \quad (8)$$

where  $n$  is the stoichiometric number of electrons involved in the reaction;  $F$  is Faraday's constant;  $C_{\text{H}_2\text{O}_2}$  is the concentration of electroactive species; and  $D_{\text{O}}$  is the diffusion constant. It can be noticed that  $|j(t)|$  falls as  $t^{-1/2}$ . From the slope of the  $|j(t)|$  vs.  $t^{-1/2}$  plot, the diffusion coefficient  $D_{\text{O}}$  of the H<sub>2</sub>O<sub>2</sub> in 0.2 M phosphate buffer is determined.  $D_{\text{O}}$  is equal to  $(4.0 \pm 0.5) \times 10^{-6} \text{ cm}^2 \text{ s}^{-1}$ . The value is slightly larger than that reported by Nasirizadeh *et al.*,<sup>28</sup> who found a value of  $2.34 \times 10^{-6} \text{ cm}^2 \text{ s}^{-1}$  measured in a 0.1 M phosphate buffer.

Fig. 5(Left) shows the CV of the HOPG surface recorded in a 0.2 M buffer phosphate pH 7 vs. Ag/AgCl at a scan rate of 0.05 V s<sup>-1</sup>. The black line corresponds to the blank voltammogram,

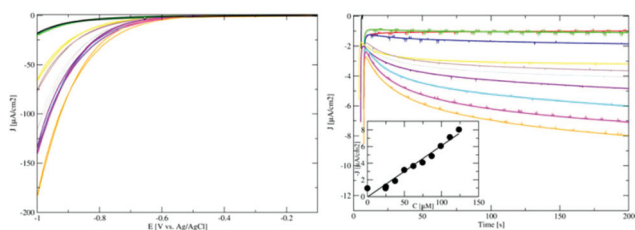


**Fig. 5** HOPG graphite working electrode in 0.2 M phosphate buffer pH 7 (Anhedra) (left) current density – potential ( $j$ - $V$ ) profiles within  $[-1; 0]$  V potential interval vs. Ag/AgCl reference electrode with a scan rate of  $0.05 \text{ V s}^{-1}$ . (Right) Current–time curve with successive addition of H<sub>2</sub>O<sub>2</sub>. The inset is the calibration curve at applied potential:  $-0.6 \text{ V}$ , illustrating the electrode response to H<sub>2</sub>O<sub>2</sub> addition. (Black line) 0.2 M buffer pH7; (red line) 12.48  $\mu\text{M}$ ; (green line) 24.94  $\mu\text{M}$ ; (blue line) 37.36  $\mu\text{M}$ ; (yellow line) 49.75  $\mu\text{M}$ ; (brown line) 62.11  $\mu\text{M}$ ; (grey line) 74.44  $\mu\text{M}$ ; (violet line) 86.74  $\mu\text{M}$ ; (light blue line) 99.01  $\mu\text{M}$ ; (magenta line) 111.25  $\mu\text{M}$ ; (orange line) 123.46  $\mu\text{M}$  of H<sub>2</sub>O<sub>2</sub> added, respectively.

which does not exhibit any redox peak. It shows the lowest current density within the potential interval  $[-1; -0.2] \text{ V}$ . The coloured lines show the  $j$ - $V$  profiles corresponding to successive injections of 50  $\mu\text{L}$  of 10 mM of H<sub>2</sub>O<sub>2</sub> into the electrochemical cell. If zoomed in between  $[-1; -0.6] \text{ V}$ , the green line shows a  $|j(t)|$  value higher than the blank. Assays were performed within the  $[12.48; 123.5] \mu\text{M}$  interval of H<sub>2</sub>O<sub>2</sub> concentrations and the density current values observed are within the  $[-200; -20] \mu\text{A cm}^{-2}$  interval.

Fig. 5(Right) shows the  $j(t)$  – time response of the HOPG/electrolyte interface, at an applied potential of  $-0.6 \text{ V vs. Ag/AgCl}$  in buffer pH 7, with the addition of 50  $\mu\text{L}$  of 10 mM H<sub>2</sub>O<sub>2</sub>. A detection limit of 12.5  $\mu\text{M}$  of H<sub>2</sub>O<sub>2</sub> is found within the 11.0–123.5  $\mu\text{M}$  interval. At short times, where the double layer charging dominates, the transient profile presents a maximum which evidences a slow kinetics for the HPRR. The steady state conditions are reached close to 120 s. At longer times, the current density reaches the limited value ( $j_{\infty}$ ). The  $j_{\infty}$  correlates with the  $C_{\text{H}_2\text{O}_2}$  according to eqn (8). The inset in Fig. 5 shows the linear response in the range 12.5–123.5  $\mu\text{M}$  fitted by linear regression giving the following equation:

$$|j(t)| \mu\text{A cm}^{-2} = -0.06616 + 0.06167 (C_{\text{H}_2\text{O}_2} \mu\text{M}) \quad (9)$$

Fig. 6(Left) shows the CV of the g-C<sub>3</sub>N<sub>4</sub>/HOPG surface recorded in 0.2 M buffer pH 7 vs. Ag/AgCl at  $0.05 \text{ V s}^{-1}$ . The black line corresponds to the blank voltammogram; it exhibits the lowest current density within the  $[-1; 0.4] \text{ V}$  potential interval. The coloured lines show the  $j$ - $V$  profiles corresponding to successive injections of 50  $\mu\text{L}$  H<sub>2</sub>O<sub>2</sub> into the electrochemical cell. Small amounts of H<sub>2</sub>O<sub>2</sub> produce significant changes in the voltammogram.

Fig. 6(Right) shows the  $j(t)$  – time response of the HOPG/g-C<sub>3</sub>N<sub>4</sub>/electrolyte interface at an applied potential of  $-0.6 \text{ V vs. Ag/AgCl}$  in buffer pH 7. The shape of the pulse is different from the HOPG one. It corresponds to a fast kinetics of HPRR. The steady state conditions were reached close to 50 s.

The effect of  $C_{\text{H}_2\text{O}_2}$  within the  $[0.05; 118] \mu\text{M}$  interval was studied. First, we added successive injections of 50  $\mu\text{L}$

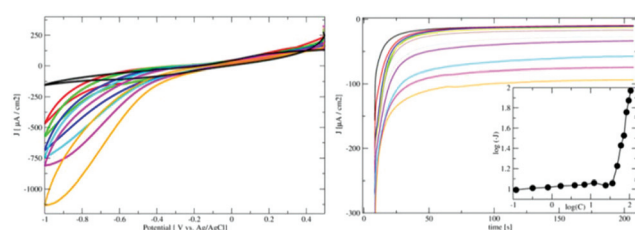


**Fig. 6** g-C<sub>3</sub>N<sub>4</sub>/HOPG graphite working electrode in 0.2 M phosphate buffer pH 7 (Anhedra) (Left) current density–potential profiles within  $[-1; 0.36] \text{ V}$  potential interval vs. Ag/AgCl reference electrode recorded at  $0.05 \text{ V s}^{-1}$  scan rate. (Right) Current–time curve with successive addition of H<sub>2</sub>O<sub>2</sub> to the 0.2 M buffer of pH 7. The inset is the calibration curve at applied potential:  $-0.6 \text{ V}$ , illustrating the electrode response to H<sub>2</sub>O<sub>2</sub> addition. (Black line) 0.2 M buffer pH 7; (red line) 0.12  $\mu\text{M}$ ; (green line) 12.26  $\mu\text{M}$ ; (blue line) 24.33  $\mu\text{M}$ ; (yellow line) 36.35  $\mu\text{M}$ ; (brown line) 48.31  $\mu\text{M}$ ; (grey line) 60.22  $\mu\text{M}$ ; (violet line) 72.06  $\mu\text{M}$ ; (light blue line) 83.85  $\mu\text{M}$ ; (magenta line) 95.58  $\mu\text{M}$ ; (orange line) 118  $\mu\text{M}$  of H<sub>2</sub>O<sub>2</sub> added, respectively.

of 0.1 mM H<sub>2</sub>O<sub>2</sub> until 12.0 μM and then successive injections of 50 μL of 10 mM H<sub>2</sub>O<sub>2</sub>. A detection limit of 0.12 μM was found.

It was surprising to find two linear behaviour regions. The inset in Fig. 6 shows the two  $j(t)$  – time linear responses corresponding to [0.12; 48.31] μM and [60.22; 118] μM concentration intervals and the linear regression fittings:

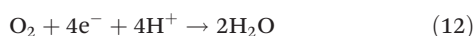
$$\log(|j(t)| \mu\text{A cm}^{-2}) = 1.02088 + 0.02428 \log(C_{\text{H}_2\text{O}_2} \mu\text{M}) \quad (10)$$

$$\log(|j(t)| \mu\text{A cm}^{-2}) = -2.12595 + 2.00714 \log(C_{\text{H}_2\text{O}_2} \mu\text{M}) \quad (11)$$

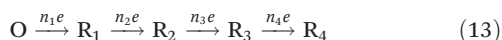
Tian *et al.*<sup>4</sup> studied a similar system, where an ultrathin g-C<sub>3</sub>N<sub>4</sub> nanosheet adsorbed on a glassy carbon electrode (g-C<sub>3</sub>N<sub>4</sub>/GCE) was analysed within a higher concentration interval between 0 to 90 mM of H<sub>2</sub>O<sub>2</sub>. Therefore, they did not find the first linear response at low concentration as in eqn (10). A nitrogen-doped carbonaceous material, like g-C<sub>3</sub>N<sub>4</sub>/GCE<sup>4</sup> or N-doped carbon nanotubes on a glassy carbon electrode (NCNT/GCE),<sup>11</sup> exhibits higher electrocatalytic performance than a carbonaceous material. Here, under steady-state conditions, the g-C<sub>3</sub>N<sub>4</sub>/HOPG electrode exhibits  $j(t)$  within the [−250.23; −22.86] μA cm<sup>−2</sup> interval for [0.12; 120] μM of H<sub>2</sub>O<sub>2</sub>, while the HOPG electrode has lower  $j(t)$  within the [−2.28; −0.28] μA cm<sup>−2</sup> interval for [12.0; 123.5] μM of H<sub>2</sub>O<sub>2</sub>.

The transient in the double-layer regions of HOPG and g-C<sub>3</sub>N<sub>4</sub>/HOPG interfaces was remarkably different. Therefore, in the next section, by means of Electrochemical Impedance Spectroscopy, we studied the structures and charge transfer processes which take place through the interfaces.

Although all the measurements were carried out with N<sub>2</sub> bubbling, where O<sub>2</sub> is completely eliminated from the electrolyte, a brief discussion of the effect of O<sub>2</sub> dissolved was also included. As expected, the O<sub>2</sub> reduction reaction (ORR) competes with HP RR at the potential studied. The ORR involves transfer of 4e<sup>−</sup> according to:



Thus there are four elementary reduction steps:



Between each of these steps, a protonation step occurs according to the following mechanism described:

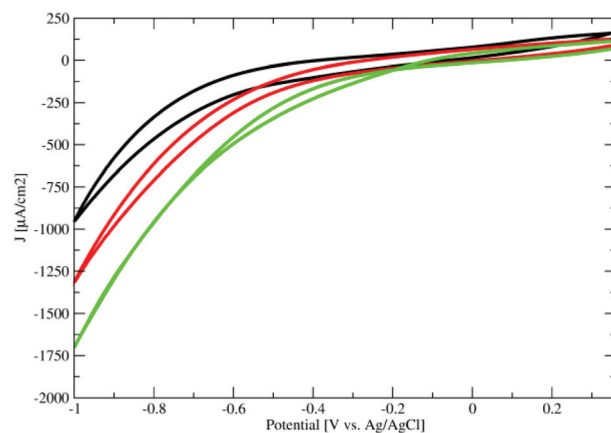
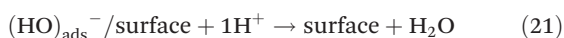
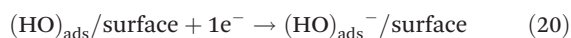
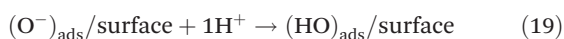
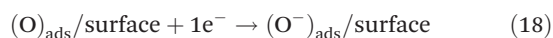
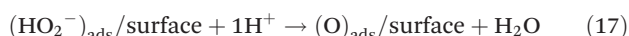
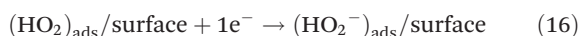
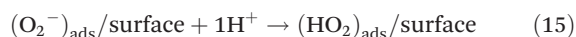
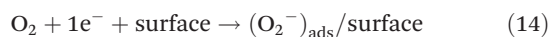


Fig. 7 Current density–potential profiles within [−1; 0.36] V potential interval vs. Ag/AgCl reference electrode recorded at 0.05 V s<sup>−1</sup> scan rate employing the g-C<sub>3</sub>N<sub>4</sub>/HOPG graphite working electrode. (Black line) 95.58 μM H<sub>2</sub>O<sub>2</sub> in 0.2 M buffer of pH 7 with N<sub>2</sub> bubble; (red line) 95.58 μM with 3 min of O<sub>2</sub> bubble; (green line) 95.58 μM with 22 min. O<sub>2</sub> bubble of H<sub>2</sub>O<sub>2</sub> added to 0.2 M phosphate buffer pH 7, respectively.

Fig. 7 shows the effect of O<sub>2</sub> present on the voltammogram. The black line corresponds to the  $|j(t)|$  – potential profile of the g-C<sub>3</sub>N<sub>4</sub>/HOPG graphite working electrode in 95.58 μM H<sub>2</sub>O<sub>2</sub> + 0.2 M phosphate buffer pH 7 without O<sub>2</sub>; the red line corresponds to 3 min of O<sub>2</sub> bubbling. It was observed that the reduction current increases due to the presence of O<sub>2</sub>. Both reactions (HP RR and ORR) occur simultaneously at the cathode. The green line was recorded after 22 min bubbling of O<sub>2</sub> and exhibited the higher reducing current found. At longer O<sub>2</sub> bubbling times, no change was observed in the voltammogram profiles. Rojas *et al.*<sup>29</sup> studied the ORR of different electrodes. It is also an interesting reaction, but in this work there are no more results presented.

### Electrochemical impedance spectroscopy (EIS) measurements

EIS allows the study and characterization of interfaces and charge transfer processes that take place through them.<sup>24,25</sup> To obtain information, the results were fitted using an equivalent circuit model. In the case of the HOPG/electrolyte interface, one Randle's circuit was employed while in the case of HOPG/g-C<sub>3</sub>N<sub>4</sub>/electrolyte interfaces, two Randle's circuits in series were used to emulate the cathode response.

One of the Randle's circuits emulates the response of the interface, including the Ohmic resistance of the solution ( $R_s$ ), the double layer response by means of a Constant Phase Element (CPE<sub>1</sub>) and the charge transfer resistance ( $R_1$ ). When the film was present, a second Randle's circuit was employed. The  $R_2$  and CPE<sub>2</sub> elements describe the film response.

The transfer function of the equivalent circuit employed<sup>25,26</sup> can be expressed as:

$$Z(\omega) = R_s + \sum_{j=1}^k \frac{R_j}{1 + (i\omega)^{n_j} R_j Q_j} \quad (22)$$

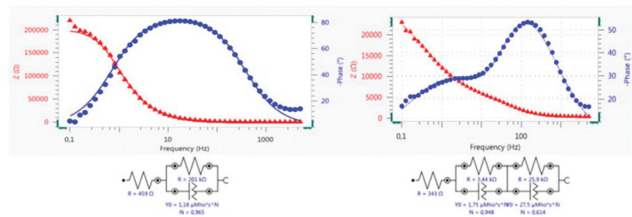


**Fig. 8** Bode plot of EIS at  $-0.6$  V vs. Ag/AgCl reference electrode of (left) HOPG/electrolyte interface buffer pH 7, (right) HOPG/g- $C_3N_4$ /electrolyte interface buffer pH 7. (Down) Equivalent circuits employed in the fitting.

where  $R_s$ ,  $R_j$  and  $Q_j$  represent Ohmic resistance, resistance and differential capacity, respectively. CPE parameters  $n_j$  and  $Q_j$  are independent of the frequency. If  $n_j$  is close to 1, the element behaves as an ideal capacitor; if  $n_j$  is close to 0.5, it represents a diffusion process through the film; and if  $n_j$  approaches zero, the film has a resistive response. Whenever  $n_j < 1$ , it indicates that the surface presents heterogeneity.<sup>30</sup>  $k$  is the number of Randle's circuits in series (1 or 2). The transfer function given by eqn (22) comprises  $k$  time-constants ( $\tau_j = R_j Q_j$ ).

As the cathode is a negatively charged electrode, in the inner Helmholtz region, there are counter-cations aligned along the electrified surface and water molecules. In the outer Helmholtz region, there are cations, anions and solvent molecules which are also present in the diffusion layer.

Electrons are transferred across the electrified interface. The charge transfer leads to both Faradaic and non-Faradaic processes. The Faradaic component arises from the electron transfer of HPRR across the interface by overcoming an appropriate activation barrier, namely the total resistance.<sup>31</sup>

Fig. 8 shows EIS measurements obtained for both interfaces in buffer pH 7. Fig. 8 left displays the Bode plot of the HOPG/electrolyte interface, which is a highly ordered surface; thus CPE<sub>1</sub> elements tend to an ideal capacitor response with the  $n$  value close to 1.

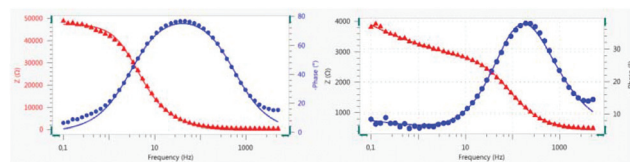
Fig. 8 right shows the Bode plot of the HOPG/g- $C_3N_4$ /electrolyte interface, which evidences two-time constants, one can be related to the heterogeneity attributed to the presence of the film deposited on the surface; the other represents the double layer. The Bode plot of the HOPG/electrolyte shows high values of the impedance module compared to that of the HOPG/g- $C_3N_4$ /electrolyte interface.

Table 2 lists the fitting parameters obtained with the equivalent circuits for both interfaces. The  $R_s$  values are similar for both electrodes. The  $R_1$  value is lower for the HOPG/g- $C_3N_4$ /electrolyte interface while  $Q_1$  and  $n_1$  remain almost constant. The exponent  $n_1$  tends to a capacitive behavior, whereas  $n_2$  indicates a diffusion process *i.e.*, approaching a value of 0.5.<sup>28</sup>

Fig. 9 shows the interfaces in the presence of  $H_2O_2$  at a potential where the Faradaic process of HPRR takes place, evidencing changes in the Bode plots as well as in the parameters of components of the equivalent circuit, listed in Table 3. The impedance module decreases with the addition of  $H_2O_2$ , which shows that the response of the interface is sensitive to

**Table 2** Fitting parameters with equivalent circuits of the EIS measured in buffer pH 7, respectively

HOPG/electrolyte	HOPG/g- $C_3N_4$ /electrolyte
$R_s$ 459 ± 8 W cm <sup>2</sup>	$R_s$ 342 ± 9 W cm <sup>2</sup>
$R_1$ 201 ± 4 kW cm <sup>2</sup>	$R_1$ 3.4 ± 0.3 kW cm <sup>2</sup>
CPE <sub>1</sub> $Q_1 = 1.18 ± 0.03$ mW <sup>-1</sup> cm <sup>-2</sup> $n_1 = 0.965 ± 0.005$	CPE <sub>1</sub> $Q_1 = 1.7 ± 0.2$ mW <sup>-1</sup> cm <sup>-2</sup> $n_1 = 0.95 ± 0.03$
	$R_2$ 25 ± 1 kW cm <sup>2</sup>
	CPE <sub>2</sub> $Q_2 = 27.5 ± 0.9$ mW <sup>-1</sup> cm <sup>-2</sup> $n_2 = 0.61 ± 0.02$



**Fig. 9** Bode plot of EIS at  $-0.6$  V vs. Ag/AgCl reference electrode of (left) HOPG/electrolyte interface buffer pH 7 + 86.74  $\mu$ M  $H_2O_2$ , (right) HOPG/g- $C_3N_4$ /electrolyte interface buffer pH 7 + 82.64  $\mu$ M  $H_2O_2$ .

**Table 3** Fitting parameters with equivalent circuits of the EIS measured in buffer pH 7 with the addition of 86.74  $\mu$ M of  $H_2O_2$  and 82.64  $\mu$ M of  $H_2O_2$ , respectively

HOPG/electrolyte	HOPG/g- $C_3N_4$ /electrolyte
$R_s$ 341 ± 7 $\Omega$ cm <sup>2</sup>	$R_s$ 323 ± 9 $\Omega$ cm <sup>2</sup>
$R_1$ 47.2 ± 0.7 k $\Omega$ cm <sup>2</sup>	$R_1$ 2.02 ± 0.08 k $\Omega$ cm <sup>2</sup>
CPE <sub>1</sub> $Q_1 = 1.36 ± 0.05$ $\mu\Omega^{-1}$ cm <sup>-2</sup> $n_1 = 0.942 ± 0.006$	CPE <sub>1</sub> $Q_1 = 2.171 ± 0.2$ $\mu\Omega^{-1}$ cm <sup>-2</sup> $n_1 = 0.91 ± 0.02$
	$R_2$ 18.37 ± 0.08 k $\Omega$ cm <sup>2</sup>
	CPE <sub>2</sub> $Q_2 = 639.3 ± 0.2$ $\mu\Omega^{-1}$ cm <sup>-2</sup> $n_2 = 0.24 ± 0.02$

the  $H_2O_2$  concentration. Fig. 9 – left shows the Bode plot of the HOPG/electrolyte interface with only one-time constants, while Fig. 9 – right shows the corresponding Bode plot of the HOPG/g- $C_3N_4$ /electrolyte interface. In this case, there are two-time constants which are not evident, ( $\tau_1 = R_1 Q_1$ ) and ( $\tau_2 = R_2 Q_2$ ), and can be detected from the circuit fitting. Therefore, one of the time-constants is associated with the electron transfer process through the g- $C_3N_4$  film and the other with the double layer region, according to the electron transfer steps described for HPRR (eqn (3)–(5)) which involve the surface.

We know that g- $C_3N_4$  is a semiconductor material with a band gap of 1.90 eV;<sup>7</sup> hence, surprisingly, when the film was present, we found a decrease in the total resistance and a shift in time constant with the increase of  $H_2O_2$  concentration.

Fig. 10, left shows that the total resistance is equal to  $R_{Total}^{HOPG/elect.} = R_1$  or  $R_{Total}^{HOPG/g-C_3N_4/elect.} = R_1 + R_2$  obtained from the fitting of the experimental data as a function of  $H_2O_2$  concentration.

In the case of  $R_{Total}^{HOPG/elect.}$ , the charge transfer went through a maximum between 10 and 50  $\mu$ M of  $H_2O_2$ . Afterwards, resistance decreased with the increase in  $H_2O_2$  concentration.



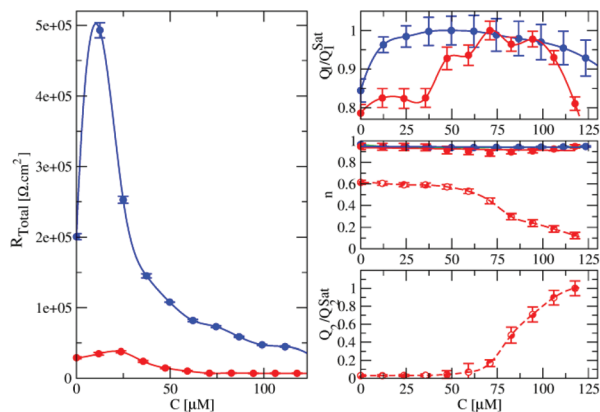


**Fig. 10** (Left) Total charge transfer resistance values; (right top and down) constant phase elements normalized to saturation value as a function of  $\text{H}_2\text{O}_2$  concentration.  $Q_1$  and  $Q_2$  are the differential capacitances of the double layer and the film, respectively; (right middle) continuous line:  $n_1$  exponent; slash line  $n_2$  exponent. (Blue) HOPG/electrolyte and (red) HOPG/ $g\text{-C}_3\text{N}_4$ /electrolyte interfaces (red and white) correspond to  $n_2$  or  $Q_2$ .

Although the HOPG/ $g\text{-C}_3\text{N}_4$ /electrolyte interface also exhibited a maximum at low concentrations, in the interval between 10 and 50  $\mu\text{M}$ , the  $R_{\text{Total}}^{\text{HOPG}/g\text{-C}_3\text{N}_4/\text{elect.}}$  values were lower than those of  $R_{\text{Total}}^{\text{HOPG}/\text{elect.}}$  over the entire range of concentrations, indicating that this surface was more electro-active than the other. When the  $g\text{-C}_3\text{N}_4$  film was present, two features were observed: the effective barrier to charge transfer through the interface was diminished; at high concentration of  $\text{H}_2\text{O}_2$ , resistance reached a constant value of 20  $\text{K}\Omega\text{ cm}^2$ , showing that the electrode response was improved by the presence of the  $g\text{-C}_3\text{N}_4$  film.

Fig. 10, right top shows the constant phase element  $\text{CPE}_1$  which describes the double layer response as a function of the analyte concentration. The  $Q_1$  parameter starts decreasing after 50  $\mu\text{M}$  and 75  $\mu\text{M}$  for HOPG/electrolyte and HOPG/ $g\text{-C}_3\text{N}_4$ /electrolyte interfaces, respectively. The red line shows  $Q_1$  fluctuations in the double layer behavior, due to periodic pore distribution and inhomogeneity present in the film. From the region between 37 and 80  $\mu\text{M}$  of  $\text{H}_2\text{O}_2$ , Fig. 10, right middle shows, for both interfaces,  $n_1$  parameters close to 1, indicating a capacitive response of the  $\text{CPE}_1$  elements. The “red and white” circle describes the  $n_2$  parameter of the  $\text{CPE}_2$  element. It changes from 0.6 to 0.2 according to the concentration. At low concentrations, the response is related to diffusion with deviations from Fick's second law.<sup>32</sup> Probably the analyte also diffuses through the film pores. At high concentrations, the  $n_2$  element approaches 0.2 indicating that the  $\text{CPE}_2$  represents distorted resistance. Fig. 10, right down shows the  $Q_2$  parameter of the  $\text{CPE}_2$  element as a function of concentration.  $Q_2$  starts increasing at concentrations higher than 75  $\mu\text{M}$  of  $\text{H}_2\text{O}_2$  in the same region where the  $n_2$  parameter changes from diffusion to a resistive behaviour.

The  $n_2$  and  $Q_2$  parameters of the  $\text{CPE}_2$  element were a function of the concentration showing the electrochemical behav-

our of the film at the HOPG/ $g\text{-C}_3\text{N}_4$ /electrolyte interface. The result shows changes in the charge transfer process on the interface which explains the two slopes observed in the calibration curve shown in Fig. 6.

## Why is the $g\text{-C}_3\text{N}_4$ /HOPG sensor more electro-catalytic than the HOPG one?

As previously mentioned, all the atoms in the  $g\text{-C}_3\text{N}_4$  structure have  $sp^2$  hybridization, which allows a graphite structure of stacked sheets. This material is an n-type organic semiconductor with a band gap of 1.90 eV,<sup>7</sup> whose Fermi level is close to the conduction band. Graphite has a band gap of 0.15 eV,<sup>7</sup> however, in certain environments, it behaves like a metal, due to its almost metallic character.<sup>33–35</sup> From the point of view of chemocatalysis, XH Li *et al.*<sup>33,34</sup> analysed the Mott-Schottky effects that modify the electronic structure of the heterojunction HOPG/ $g\text{-C}_3\text{N}_4$  through the bending of the bands. This phenomenon favours the charge transfer for the oxidation or reduction reactions. Recently, X Li *et al.*<sup>36</sup> studied the graphene/ $g\text{-C}_3\text{N}_4$  heterojunction, finding a considerable opening in the band gap, between 0.041 eV and 0.108 eV depending on sheet stacking. These band gaps are even smaller than those observed in graphite. Fig. 11 right shows the HPRR through the interface described according to the Gerisher model.<sup>31</sup> The  $g\text{-C}_3\text{N}_4$  Fermi level ( $E_f$ ) is near the conduction band. When a negative potential is applied to the electrode, the  $E_f$  is shifted until the redox potential ( $E_{\text{redox}}^0$ ) is reached, the analyte reduction begins and the semiconductor bands bend. This phenomenon favors the reaction at the  $g\text{-C}_3\text{N}_4$ /electrolyte interface. In graphite the reduction also occurs; however,  $|j(t)|$

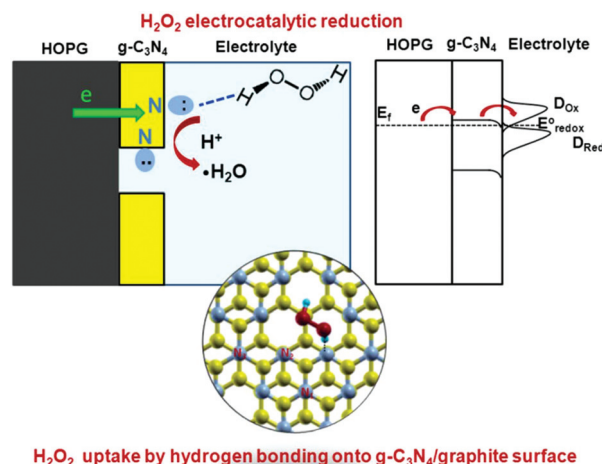


**Fig. 11** (Left) Scheme of the  $\text{H}_2\text{O}_2$  reduction reaction onto the HOPG/ $g\text{-C}_3\text{N}_4$ /electrolyte interface. (Right) Gerisher's model for the reduction reaction at the electrochemical interface.  $E_f$ ,  $E_{\text{redox}}^0$ ,  $D_{\text{Ox}}$ , and  $D_{\text{Red}}$  are Fermi level, redox potential, and state distribution of oxidized and reduced species, respectively. (Down)  $\text{N}_1$ ,  $\text{N}_2$ , and  $\text{N}_3$  are the different adsorption sites. C: yellow sphere; N: gray sphere; O: red sphere; H: light blue sphere.



**Table 4** Adsorption of H<sub>2</sub>O<sub>2</sub> on the g-C<sub>3</sub>N<sub>4</sub>/graphene surface. Site type, Mulliken atomic charge [atomic unit], adsorption energy [eV], and lone pair

Site	Q <sub>N</sub> [a.u.]	E <sub>ads</sub> [eV]	Lone pair
N <sub>1</sub>	0.218	-0.80	P
N <sub>2</sub>	0.262	-0.86	sp <sup>2</sup>
N <sub>3</sub>	0.452	-0.69	P

values were significantly lower. The reaction was more impeded due to lower H<sub>2</sub>O<sub>2</sub> uptake on HOPG.

Fig. 11 left shows a scheme of the H<sub>2</sub>O<sub>2</sub> adsorptions on the HOPG/g-C<sub>3</sub>N<sub>4</sub>/electrolyte interface.

The origin of the surprising selectivity and electrocatalytic activity of the g-C<sub>3</sub>N<sub>4</sub>/HOPG sensor is attributed to the chemical nature of tri-*s*-triazine units. The g-C<sub>3</sub>N<sub>4</sub> sheets comprise N atoms which, unlike C atoms, have a lone electron pair. In the g-C<sub>3</sub>N<sub>4</sub> structure, there are three types of N atoms with different environments: those with a lone pair in the sp<sup>2</sup> orbital and those with a lone pair in the p orbital<sup>37</sup> (Fig. 1). This feature allows the surface a huge uptake of H<sub>2</sub>O<sub>2</sub> molecules through hydrogen bonding. This is a major advantage over graphite or graphene where H<sub>2</sub>O<sub>2</sub> adsorption is more impeded and C atoms should lose part of their sp<sup>2</sup> hybridization and their aromatic character to allow adsorption, displaying particularly low adsorption energy values -0.05 eV.<sup>14</sup>

We performed some calculation at the DFT level to study H<sub>2</sub>O<sub>2</sub> adsorption on the g-C<sub>3</sub>N<sub>4</sub>/graphene bilayer. Table 4 lists E<sub>ads</sub><sup>g-C<sub>3</sub>N<sub>4</sub>/graphene</sup> values. They are significantly higher than those reported for graphene.<sup>14</sup> The preferential site corresponds to N<sub>2</sub> with an energy value of -0.86 eV. In order to calculate coverage ( $\theta$ ) and surface concentration (C<sub>s</sub>), equilibrium conditions at the surface were assumed:  $\mu_{\text{sol}}^{\text{H}_2\text{O}_2} = \mu_{\text{ad}}^{\text{H}_2\text{O}_2}$ .

In order to have a rough estimation, only the translational contribution to  $\mu_{\text{sol}}^{\text{H}_2\text{O}_2}$  is considered, and a non-interacting lattice gas adsorbed was assumed at the coverage  $\theta$ .<sup>38</sup>

$$-kT \ln \left[ \left( \frac{2\pi mkT}{h^2} \right)^{3/2} \frac{V}{N} \right] = kT \ln \left( \frac{\theta}{1-\theta} \right) + E_{\text{ads}} \quad (23)$$

where  $k$  denotes the Boltzmann constant,  $m$  is the mass of the molecule,  $C_{\text{H}_2\text{O}_2} = N/V$  and  $h$  is the Planck constant.  $\theta$  can be obtained from eqn (23):

$$x = \exp \left( \frac{\mu_{\text{sol}}^{\text{H}_2\text{O}_2} - E_{\text{ads}}}{kT} \right) \quad (24)$$

$$\theta = \frac{x}{1+x} \quad (25)$$

Table 5 shows the C<sub>s</sub><sup>3/2</sup>/C<sub>H<sub>2</sub>O<sub>2</sub></sub> ratio, C<sub>s</sub> and C<sub>H<sub>2</sub>O<sub>2</sub></sub> are the surface and bulk concentration, respectively. This ratio should give an idea of the adsorption extent at each bulk concentration. We can see that the E<sub>ads</sub> difference gives HOPG a lower coverage, while for g-C<sub>3</sub>N<sub>4</sub>/HOPG, the surface is covered almost completely. On the other hand,  $\theta$  and C<sub>s</sub> are sensitive to C<sub>H<sub>2</sub>O<sub>2</sub></sub>, also seen in the transients of Fig. 5 and 6.

**Table 5** Coverage degree ( $\theta$ ) and ratio C<sub>s</sub><sup>3/2</sup>/C<sub>H<sub>2</sub>O<sub>2</sub></sub>, where C<sub>s</sub> is the surface concentration of adsorbed molecules, gives a measure for the enhancement of the local concentration of the analyte due to the presence of the surface

C <sub>H<sub>2</sub>O<sub>2</sub></sub> [μM]	HOPG		g-C <sub>3</sub> N <sub>4</sub> /HOPG	
	$\theta$	C <sub>s</sub> <sup>3/2</sup> /C <sub>H<sub>2</sub>O<sub>2</sub></sub>	$\theta$	C <sub>s</sub> <sup>3/2</sup> /C <sub>H<sub>2</sub>O<sub>2</sub></sub>
0.12	2.65 × 10 <sup>-12</sup>	2.19 × 10 <sup>-15</sup>	0.9925	3.49
12.00	2.65 × 10 <sup>-10</sup>	2.19 × 10 <sup>-14</sup>	0.9999	3.49
120.00	2.65 × 10 <sup>-9</sup>	6.93 × 10 <sup>-14</sup>	0.9999	0.35

## Conclusions

The aim of the present work was to develop an efficient green biosensor for the detection and quantification of H<sub>2</sub>O<sub>2</sub>. A comparative study between HOPG and g-C<sub>3</sub>N<sub>4</sub>/HOPG sensors was carried out. The g-C<sub>3</sub>N<sub>4</sub>/HOPG electrode shows the best electro-active performance for H<sub>2</sub>O<sub>2</sub> quantification.

First, graphitic carbon nitride was synthesized by heat treatment of melamine. The product was a tri-*s*-triazine polymer, one of the g-C<sub>3</sub>N<sub>4</sub> allotropes, obtained with a yield of 75 wt%. The g-C<sub>3</sub>N<sub>4</sub> was characterized by spectroscopic techniques. The composition was evaluated by EDS and the crystallinity by XRD diffraction, which supported the fact that tri-*s*-triazine-based-connection patterns were obtained. In order to form the g-C<sub>3</sub>N<sub>4</sub> ultrathin film on the HOPG surface, g-C<sub>3</sub>N<sub>4</sub> was successfully exfoliated in an acid medium under sonication; an ethanolic suspension was then prepared with them. Finally, the film was grown drop-wise from that suspension.

In the electrochemical characterization of the sensor,  $j(t)$ -time curves were recorded at -0.6 V vs. the Ag/AgCl reference electrode, in the range of low H<sub>2</sub>O<sub>2</sub> concentration by means of successive addition.

For the g-C<sub>3</sub>N<sub>4</sub>/HOPG sensor, we found a higher electrocatalytic activity and a lower detection limit compared to those seen in the HOPG one. The g-C<sub>3</sub>N<sub>4</sub>/HOPG electrode reached faster the steady state condition than the HOPG one, with different qualitative and quantitative behaviour. Particularly, the g-C<sub>3</sub>N<sub>4</sub>/HOPG sensor has analytical stability and reproducibility, allowing reliable and sensitive determination of low H<sub>2</sub>O<sub>2</sub> concentration until a detection limit of 0.12 μM.

EIS measurements were also performed at a potential of -0.6 V where the Faradaic process of HPRR took place. For the entire range of concentrations studied, at the HOPG sensor, the reaction occurred with a higher charge transfer resistance than that at the g-C<sub>3</sub>N<sub>4</sub>/HOPG sensor.

This behavior is associated with the chemical and physical properties of the sensor. The g-C<sub>3</sub>N<sub>4</sub>/HOPG surface, due to the N content, allows high uptake of H<sub>2</sub>O<sub>2</sub>. The heterojunction leads to a change in the electronic structure which favors the charge transfer process through the bending of the bands.

This is the first study conducted in depth. With all the results shown, we can affirm that g-C<sub>3</sub>N<sub>4</sub>/HOPG is an efficient, low-cost and environmentally friendly sensor for H<sub>2</sub>O<sub>2</sub> quanti-

fication. It allows an accurate and efficient determination of low H<sub>2</sub>O<sub>2</sub> concentration.

## Acknowledgements

This work was supported by CONICET PIP-11220120100031, PIP-11220110100499, PIP-11220100100411, PIO-15920150100013CO and SeCyT-UNC. A. M. Silva would like to thank INMETRO for the postdoctoral fellowship. The authors also wish to acknowledge language assistance by C. Mosconi.

## Notes and references

- 1 M. Groenewolt and M. Antonietti, *Adv. Mater.*, 2005, **17**, 1789–1792.
- 2 B. Jürgens, E. Irran, J. Senker, P. Kroll, H. Müller and W. Schnick, *J. Am. Chem. Soc.*, 2003, **125**, 10288–10300.
- 3 A. Thomas, A. Fischer, F. Goettmann, M. Antonietti, J. Oliver Müller, R. Schlögl and J. M. Carlsson, *J. Mater. Chem.*, 2008, **18**, 4893–4908.
- 4 J. Tian, Q. Liu, C. Ge, Z. Xing, A. M. Asiri, A. O. Al-Youbi and X. Sun, *Nanoscale*, 2013, **5**, 8921–8924.
- 5 D. M. Teter and R. J. Hemley, *Science*, 1996, **271**, 53–55.
- 6 M. E. Straumanis, *J. Appl. Phys.*, 1959, **30**, 1965–1969.
- 7 A. M. Silva and M. I. Rojas, *Comput. Theor. Chem.*, 2016, **1098**, 41–49.
- 8 M. Ovcharov, N. Schcheerban, S. Filonenko, A. Mishura, M. Skoryk, V. Shvalagin and V. Granchak, *Mater. Sci. Eng., B*, 2015, **202**, 1–7.
- 9 S. N. Guo, Y. Zhu, Y. Y. Yan, Y. L. Min, J. C. Fan and Q. Xu, *Appl. Catal., B*, 2016, **185**, 315–321.
- 10 F. Goettman, A. Fischer, M. Antonietti and A. Thomas, *Chem. Commun.*, 2006, 4530–4532.
- 11 X. Xu, S. Jiang, Z. Hu and S. Liu, *ACS Nano*, 2010, **4**, 4292–4298.
- 12 P. Du, P. Wu and C. Cai, *J. Electroanal. Chem.*, 2008, **624**, 21–26.
- 13 J. Wang, *Chem. Rev.*, 2008, **108**, 814–825.
- 14 G. L. Luque, M. I. Rojas and E. P. M. Leiva, *Electrochim. Acta*, 2010, **56**, 523–530.
- 15 A. J. Stone and D. J. Wales, *Chem. Phys. Lett.*, 1986, **128**, 501–503.
- 16 P. Giannozzi, *et al.*, *J. Phys.: Condens. Matter*, 2009, **21**, 395502–395521.
- 17 J. P. Perdew, K. Burke and M. Ernzerhof, *Phys. Rev. Lett.*, 1996, **77**, 3865.
- 18 L. Kleinman and D. M. Bylander, *Phys. Rev. Lett.*, 1982, **48**, 1425.
- 19 H. J. Monkhorst and J. D. Pack, *Phys. Rev. B: Solid State*, 1976, **13**, 5188.
- 20 Y. Bu, Z. Chen, J. Yu and W. Li, *Electrochim. Acta*, 2013, **88**, 294–300.
- 21 N. W. Ashcroft and N. D. Mermin, *Solid State Physics*, United States, 1976, p. 96 ff.
- 22 Q. Guo, Y. Xie, X. Wang, S. Lv, T. Hou and X. Liu, *Chem. Phys. Lett.*, 2003, **380**, 84–87.
- 23 Y. Yuan, L. Zhang, J. Xing, M. I. Utama, X. Lu, K. Du, Y. Li, X. Hu, S. Wang, A. Genç, R. Dunin-Borkowski, J. Arbiol and Q. Xiong, *Nanoscale*, 2015, **7**, 12343–12350.
- 24 X. Zhang, X. Xie, H. Wang, J. Zhang, B. Pan and X. Xie, *J. Am. Chem. Soc.*, 2013, **135**, 18–21.
- 25 J. Tian, Q. Liu, A. M. Asiri, A. O. Al-Youbi and X. Sun, *Anal. Chem.*, 2013, **85**, 5595–5599.
- 26 D. Das, S. L. Shindle and K. K. Nanda, *ACS Appl. Mater. Interfaces*, 2016, **8**, 2181–2186.
- 27 A. J. Bard and L. R. Faulkner, *Electrochemical Methods. Fundamentals and Applications*, John Wiley and Sons, 1980, ch. 5.
- 28 N. Nasirizadeh, Z. Shekari, A. Nazari and M. Tabatabaee, *J. Food Drug Anal.*, 2016, **24**, 72–82.
- 29 M. I. Rojas, M. J. Esplandiu, L. B. Avalor, E. P. M. Leiva and V. A. Macagno, *Electrochim. Acta*, 1998, **43**, 1785–1794.
- 30 B. Hirschorn, M. E. Oranzem, B. Tribollet, V. Vivier, I. Frateur and M. Musiani, *Electrochim. Acta*, 2010, **55**, 6218–6227.
- 31 B. Y. Chan and S. M. Park, *Annu. Rev. Anal. Chem.*, 2010, **3**, 207–229.
- 32 X. Yuan, C. Song, H. Wang and J. Zhang, *Electrochemical Impedance Spectroscopy in PME Fuel Cells: Fundamentals and Applications*, Springer-Verlag, London, 2010, pp. 140–142.
- 33 X. H. Li and M. Antonietti, *Chem. Soc. Rev.*, 2013, **42**, 6593–6604.
- 34 X. H. Li, J. S. Chen, X. Wang, J. Sun and M. Antonietti, *J. Am. Chem. Soc.*, 2011, **133**, 8074–8077.
- 35 N. Sato, *Electrochemistry at Metal and Semiconductor Electrodes*, Elsevier, Amsterdam, 1998.
- 36 X. Li, Y. Dai, Y. Ma, S. Han and B. Huang, *Phys. Chem. Chem. Phys.*, 2014, **16**, 4230–4235.
- 37 J. McMurry, *Organic Chemistry*, Cengage Learning, México, 8th edn, 2012, p. 976.
- 38 T. L. Hill, *Introduction to Statistical Thermodynamics*, Dover Publication, Inc., New York, 1986, pp. 124–130.